APEM journal
Advances in Production Engineering & Management
Volume 18 | Number 1 | March 2023 | pp 49–65
https://doi.org/10.14743/apem2023.1.456
ISSN 1854-6250
Journal home: apem-journal.org
Original scientific paper

Spatial position recognition method of semi-transparent and flexible workpieces: A machine vision based on red light assisted

Bi, Q.L.[a], **Lai, M.L.**[b,*], **Chen, K.**[b], **Liu, J.M.**[b], **Tang, H.L.**[b], **Teng, X.B.**[a], **Guo, Y.Y.**[a]

[a]School of Marine Engineering, Guangzhou Maritime University, Guangzhou, P.R. China
[b]School of physics and optoelectronic Engineering, Guangdong University of Technology, Guangzhou, P.R. China

ABSTRACT

In the automatic sorting process, overlapping translucent and flexible workpieces on the conveyor belt, blurring the imaging edge features of translucent and flexible workpieces is a challenge to locate the upper and lower workpieces spatially, we propose a method for locating translucent and flexible workpieces spatially under the overlapping environment in conjunction with the most common automatic sorting of translucent and flexible workpieces such as infusion tube drip buckets. Firstly, we propose a rectangular surface light source based on 650 nm band and monocular CCD for imaging translucent workpieces such as infusion tube drip buckets and optimize the imaging parameters. Secondly, we study a feature matching recognition algorithm for flexible workpieces that are prone to deformation, construct a mapping relationship between the position of overlapping layers and imaging quality of translucent and flexible workpieces such as infusion tube drip buckets based on clarity and information entropy, and establish The mapping relationship between the position of the overlapping layers and the imaging quality of translucent and flexible workpieces such as infusion tube drip buckets is constructed based on clarity and information entropy, and a local spatial coordinate conversion model is established. Finally, the spatial positioning coordinates of overlapping and non-overlapping translucent and flexible workpieces in the local coordinate system are identified, and the results show that the imaging method and theory can be effectively applied to the identification of overlapping and spatial positioning coordinates in the automatic sorting of translucent workpieces such as infusion tube drip buckets.

ARTICLE INFO

Keywords:
Machine vision;
Image processing;
Visual recognition;
Feature matching;
Imaging quality;
Red light;
Translucent and flexible workpieces;
Infusion tube drip bucket;
Smart manufacturing

**Corresponding author:*
2112115045@mail2.gdut.edu.cn
(Lai, M.L.)

Article history:
Received 14 March 2023
Revised 12 April 2023
Accepted 15 April 2023

1. Introduction

In the fields of food processing [1], manufacturing job-shops [2], health care, electrical and electronics, architectural design, and resource recovery [3], sorting means have been automated, especially for translucent flexible workpieces. Translucent and flexible workpieces such as infusion tubes and drip buckets (abbreviated as TFW-TDB) occupy a larger market for medical products (13 billion tubing and drip buckets are used annually in the Chinese medical field [4]). For the reason of used in medical, their sorting and assembly processes have more stringent standards and specification systems than other similar products [5, 6].

Machine vision has flourished and applied well in modern sorting systems for detection and sorting, and automated mechanical technology for control [7, 8]. Accurate workpiece posture

information is a prerequisite for accurate sorting by automated machines, mechanical grippers can be guided quickly and accurately to carry out grasping work, thus achieving the purpose of sorting [9]. When there is a large number of targets, it is also necessary to judge the spatial position of each target and select the most suitable workpiece among the stacked workpieces. Therefore, visual recognition and position detection technology is one of the key technologies in the field of machine vision automation [10, 11].

As early as the 1950s and 1960s, foreign research was conducted on the recognition and understanding of two-dimensional images and the recovery and coordinate mapping of three-dimensional images, and its application scenarios included aerial images [12], workpiece surface defect detection [13]. By the 1980s and 1990s, CCD and CMOS camera technology progressed rapidly [14], and machine vision technology was better supported. China started late in this area, but has achieved good results in various fields. The most popular method for a large number of target recognition is template matching [15, 16], which is widely used in various fields such as license plate detection [17], fingerprint recognition [18], font recognition [19, 20], distance estimate [21]and even waveform classification [22] by virtue of its simplicity, stability, and accuracy. However, the following challenges exist in imaging the characteristics of TFW-TDB. (1) Blurred edges: Its translucent nature makes the edge features of TDB in imaging inconspicuous, which will affect the performance of the image algorithm and lead to difficulties in distinguishing spatial relationships when multiple TDB overlap; (2) Flexible and easily deformed: TDB are too soft and the stacked workpieces are prone to deformation during the sorting process, making it more difficult to accurately identify their positioning coordinates. Therefore, the sorting and assembling of TDB is still done manually, which makes it difficult to control the efficiency and quality effectively in the long run. Therefore, we propose a method that can be adapted to the inspection of workpieces with this feature. Since the object-oriented objects in this paper are standard artifacts, the template matching method is considered. Template matching is performed by creating a template similar to the target image, translating, rotating, and 3D transforming the template image to overlap with the target image as much as possible, and then quantifying the comprehensive similarity degree by comparing the pixels of each point in the overlap region, corner features and light and shadow changes. When the similarity degree is higher than a set threshold, the target is recognized and the spatial pose information of the target is returned.

The mode of image pixel matching and image feature matching are two common template matching methods. The former matches the template pixels directly with the pixels of the image to be measured, while the latter constructs a template by finding the relationship between the target features and the coordinates of the corner points, and then extracts the features of the measured image for matching. Korman *et al*. [23] proposed a matching algorithm capable of performing arbitrary affine transformations by calculating the sum of the absolute differences between the template and the affine changed region and finding the minimum value for matching, but this process is only effective for the deformation on the perspective, and will result in large errors if the target sample itself changes. Zhang *et al*. [24] solve the problem that the original template matching method based on NCC (normalized correlation) is too slow for rotated images, and propose a sub-NCC-based template matching method, which selects rotationally invariant edge points from rotationally invariant pixels and uses the selected points for rough matching to quickly filter out the mismatched regions, improving the anti-interference ability and matching speed of the algorithm. Zhang *et al*. [25] proposed a multi-scale template matching method based on nearest neighbour (NN) search, which provides scale adaption by extending the diversity similarity DIS and explicitly penalizing deformation to deal with the situation that the size of the candidate window is fixed and cannot solve the object scale changes greatly. Experiments show that the proposed method is robust in terms of extended variation as well as other challenging aspects and outperforms state-of-the-art methods using both colour and depth features. Ye *et al*. [26] proposed a fast and robust template matching framework integrating local descriptors of multimodal images to cope with the multimodal data problem, and proposed a novel pixel feature for images using oriented gradients (CFOG) with excellent performance in image matching and computational efficiency. Consider the disadvantages of the existence of over-segmentation and image interference by reflected light, Wu and Li [27] proposed an improved watershed algorithm based on morphological gradients. The method obtains the component gradients of colour images in a

new colour space without interference from reflected light. The gradient image is reconstructed by turning on and off, and the final gradient image is obtained. Additionally, deep learning-based matching algorithms are the mainstream in recent years. Wang *et al*. [28] proposed such algorithm to achieve the recognition of different types of track profiles. The template-matching driven spatio-temporal context tracking algorithm is used to achieve fast tracking of laser stripes on the rail head. The method effectively solves the problem of profile measurement of passing trains at the crossing, and achieves precise positioning and fast tracking of various types of laser stripes. Hikosaka and Tonooka [29] proposed a new method for automatic image-to-image alignment, which performs image-to-image alignment by applying template matching to road masks extracted from images using a two-step deep learning model. Chen *et al*. [30] proposed a new MC-UNet, which expands the depth of MC-UNet layer to 2 layers and reduces the maximum number of channels to 32/31 compared to the classical U-Net. Using average pooling and embedding channel attention in the hopping process between encoder and decoder layers of the same network depth, the computational speed and accuracy are improved.

In the actual production process, the spatial relationship of the target under the camera still needs to be clarified. Especially in the stacked state, it is more difficult to achieve matching when there is a target that is partially occluded. Currently, there is a class of methods to determine the part space relationship by calculating the edge integrity. In the edge extraction algorithm, Sangeetha and Deepa [31] improved on the basis of Canny algorithm and proposed a new Canny algorithm without any loss in detecting edges at the block level to solve the traditional. The edge detection method is complex, time-consuming, and has high hardware cost. Goyal *et al*. [32] proposed an improved version of local binary mode LBP, namely ILBP, to overcome the limitations of basic LBP.ILBP replaces the fixed weighting matrix of basic LBP with a pixel difference matrix. Results show that ILBP has superior performance and is very effective for noisy, blurred and low pixel value images. Mittal *et al*. [33] proposed a robust edge detection algorithm using a multi-thresholding approach (B-Edge) to compensate for the edge connectivity and edge thickness problems encountered in edge detection, and successfully detected robust and continuous thin edges with a small percentage of noise. Furthermore, there is also the use of three-dimensional reconstruction to make judgments, and such methods are more accurate although the computational complexity of the algorithm is increased. He *et al*. [34] solve the problem of overlapping and mixing workpieces, which makes it difficult for robotic arms to grasp workpieces. Take advantage of 3D laser scanner to obtain the point cloud features of the workpiece. The point cloud is first filtered and segmented, and then fed into RS-CNN network for recognition and classification. According to result, different models are used to record the point clouds in the scene. Finally, the final pose of the workpiece to be grasped is obtained to realize the unordered grasping of various workpieces. Chen *et al*. [35] proposed a novel stereo matching algorithm combining polar geometry and cross ratio invariance (CMEC) to reconstruct the workpiece in 3D by fitting the plane with least squares. The matching accuracy reaches 3 % and the measurement accuracy reaches 99.0 mm. Wang [36] proposed an improved LIDAR point cloud surface reconstruction algorithm to achieve fast 3D surface reconstruction from a given scattered point cloud. The idea of classification is also incorporated into template matching and 3D reconstruction to better obtain the spatial information of stacked parts.

With the continuous development of neural networks, deep learning-based methods are becoming more and more mature, which has become an important trend in the field of sorting. Han and Han [37] proposed a detection method based on an improved Faster R-CNN model, improved the Faster R-CNN feature network, and selected ResNet combined with SENet for feature extraction, which improved the important feature layer and suppressed the non-significant feature layer is suppressed. The Soft-NMS algorithm was introduced to optimize the NMS algorithm to reduce the problem of missed and false detection of overlapping or adjacent targets. Li *et al*. [38] proposed an improved artifact recognition method based on YOLOV5. By adding an attention module to the backbone network, the feature extraction capability of the network is enhanced. Secondly, the SIoU loss function is used to speed up the convergence speed, improve the regression accuracy and enhance the network accuracy. The phenomenon of missed detection, false detection and overlap can be effectively avoided.

In the infusion tube processing process, the material is flexible, translucent and other physical properties, the general machine vision feature matching algorithm is difficult to cope with, the biggest problem is that the infusion tube valve bubble itself is not fixed. General template matching algorithm can only be applied to the traditional perspective deformation, when the measured target itself deformation is difficult to identify; and deep learning algorithms are generally more complex, hardware chips and data sets require a certain cost to build, real-time is also relatively poor.

When it comes to the overlapping grasping of the infusion tube valve bubble, considering that the infusion tube valve bubble is not a perfectly straight line, as well as for its translucent nature characteristic, the exact edge position of the bubble extracted using the general edge detection algorithm is limited, it leads to a large error between the center of the workpiece and the grasping point. At the same time, the complexity of the algorithm based on 3D reconstruction and deep learning is too high, and it is difficult for ordinary embedded chips to achieve real-time detection, so most of them are not applicable to the application scenario of the spatial positioning of the infusion tube valve bubble in this paper.

Therefore, we propose a visual recognition method for the infusion tube valve bubbles; our method is improved and designed as follows.

- Adopt backlighting for overexposure type illumination, and use contrasting red light to solve the problem of unstable imaging quality of infusion tube valve bubbles in overlapping state.
- An improved template matching algorithm based on deformation is proposed, and reasonable matching greediness and distortion thresholds are set to realize the segmentation and identification and localization operations of infusion tube valve bubbles in the overlapping state.
- To construct a coupled model of spatial position and imaging quality of infusion tube valve bubbles by using clarity coefficient and information entropy to realize the determination of spatial position of infusion tube valve bubbles.

2. The principle and methods

2.1 Composition of TFW-TDB visual positioning system

The TFW-TDB vision positioning system is mainly composed of conveyor conveying subsystem, sorting actuator, optical imaging subsystem, information processing subsystem and motion control subsystem (shown in Fig. 1). The optical imaging system consists of CCD camera, auxiliary light source, and imaging posture adjustment mechanism. In the TFW-TDB imaging on the conveyor subsystem, although the coaxial light source and other methods can image the TFW-TDB better and reduce the interference between the imaging device and the sorting execution device, there are problems such as insufficient contrast of edge features and difficulty in judging the upper and lower layers of overlapping features in the TFW-TDB imaging process. Therefore, the back-projected rectangular red light source backup drug-assisted imaging. the working principle of the visual positioning system in the TFW-TDB sorting process is as follows.

Firstly, the conveyor belt in the conveyor belt transport subsystem is set to transparent color, and the TFW-TDB is continuously transported by the conveyor belt to the preset imaging position, and the CCD obtains the TFW-TDB image on the conveyor belt according to the fixed adoption frequency with the assistance of the light source. Secondly, the dynamic feature matching algorithm and the TFW-TDB overlap layer determination algorithm are used to obtain the feature points in the coordinate system of the TFW-TDB image Secondly, the dynamic feature matching algorithm and TFW-TDB overlap layer determination algorithm are used to obtain the feature points in the coordinate system of TFW-TDB image and the overlap layer of TFW-TDB. Finally, the spatial positioning coordinates in TFW-TDB sorting are obtained by combining the positioning coordinates of TFW-TDB feature points in the image coordinate system, the camera calibration parameters and the mapping relationship between the measurement point coordinates and the sorting global coordinate system.

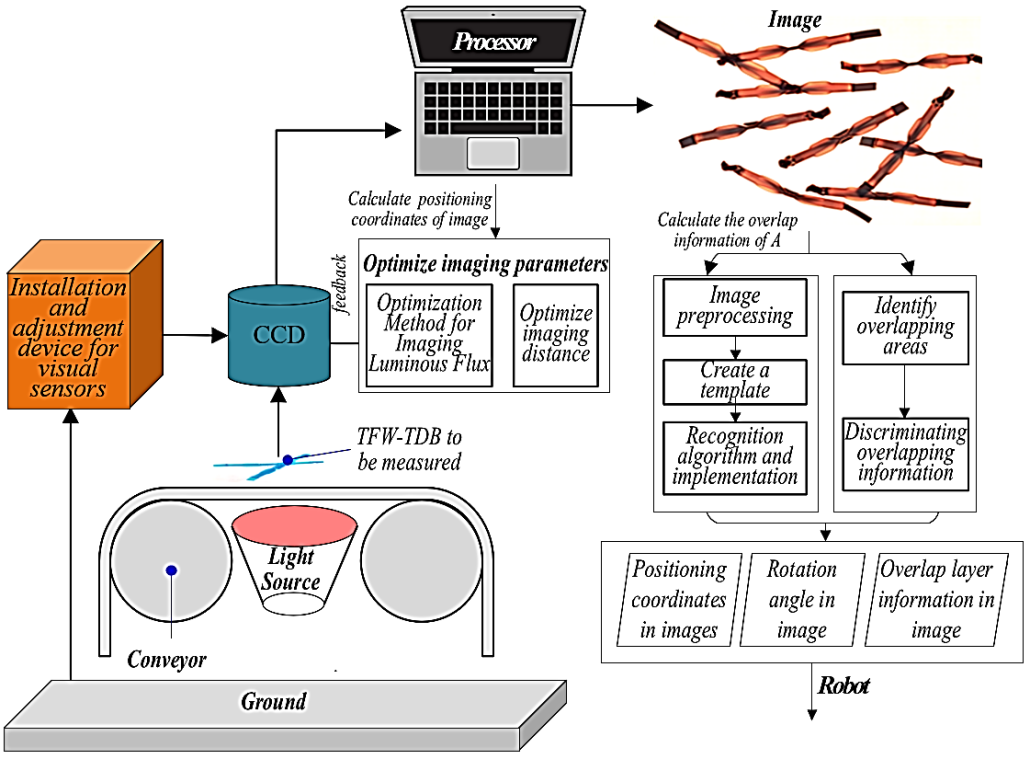

Fig. 1 Schematic diagram of TFW-TDB visual recognition system

2.2 Optimization of TFW-TDB vision system parameters

TFW-TDB imaging system is composed of CCD, auxiliary light source, light source controller, industrial control machine, transparent conveyor belt and other modules. For liquid tube drip bucket, which are easy to overlap on the conveyor belt, the back-projection type of auxiliary light illumination is proposed (shown in Fig. 1). In the imaging process, the light intensity directly affects the prominence of features in TFW-TDB imaging, reasonable imaging distance parameters can ensure TFW-TDB images each layer clearly under overlapping conditions and the features of interest occupy the highest pixel density, the TFW-TDB imaging light flux and imaging distance parameters are optimized.

A) Establishment of lighting system luminous flux optimization method

To output clear edge imaging of TFW-TDB and reduce background interference, we objectively judge the imaging results of the infusion tube drip bucket based on the information entropy image information evaluation index with the rule, that the greater the information entropy in the image, the more information the image contains [39]. The optimization method of imaging parameters in terms of information entropy is as follows:

We assume that the acquired image of the TFW-TDB region is $Image_1$, in which the gray values of each pixel point are independent of each other, its binarized distribution is as follows:

$$rel = \{rel_0, rel_1, \dots, rel_i, \dots, rel_n\}, n = 1,2, \dots ,255 \quad (1)$$

where, rel_i denotes the ratio of the number of pixels with gray value i to the total number of pixels in the image. On the basis of the above equation, Eq. 2 calculates the information entropy of $Image_1$:

$$Ent = -\sum_{0}^{n} rel_i \cdot \log_2 rel_i \quad (2)$$

To investigate the effect of auxiliary light source brightness on the imaging quality of TFW-TDB, the CCD camera aperture is adjusted to the maximum, the shutter time is set to 1/20 s, and the IPC controls the light source controller through the RS232 communication port to change the brightness of the auxiliary light source, assuming that the brightness level of the auxiliary light

source is j ($j = 1, 2, 3, \ldots, 242$), the image acquired under different brightness levels j is Image_{1j}. The information entropy of TFW-TDB images acquired at different brightness levels j is recorded as Image_{1j}. The information entropy of image Image_{1j} under different luminance levels is calculated based on Eqs. 1, 2, and the curves are shown in Fig. 2. Then the curve continues to decline until the end. The reasons for the change of information entropy Ent_j under different luminance levels j are as follows: when the luminance of the auxiliary light source increases, the red backlight light source gradually overexposes the image, and the information of the surrounding environment is gradually lost, and the curve starts to decline, when the luminance level $j = 92$, the structural features of TFW-TDB gradually reveal, and the image information increases, and when the luminance level $j = 114$, the image becomes completely overexposed due to the increase of illuminance. At luminance level $j = 114$, the image becomes completely overexposed due to the increase in illuminance, so the best imaging effect is achieved at luminance level $j = 114$.

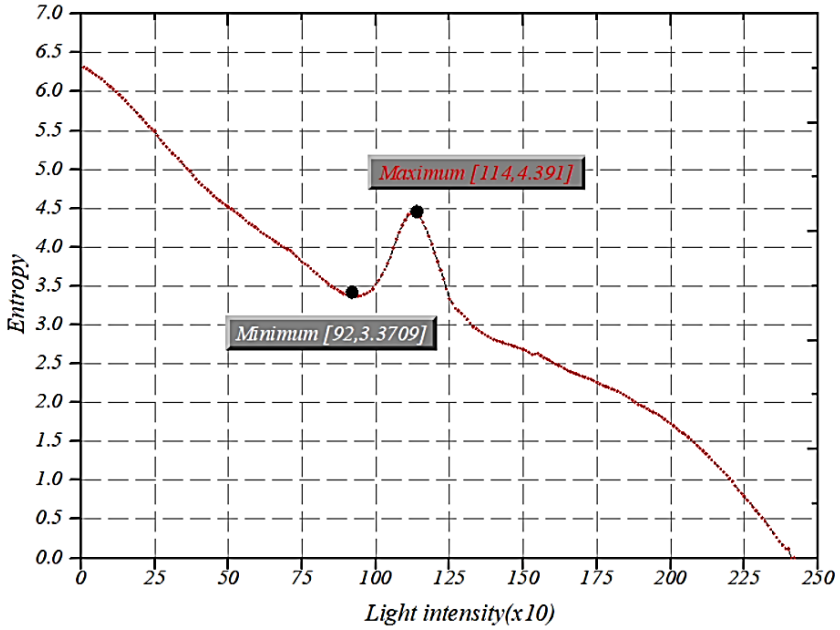

Fig. 2 Information entropy curves under different illuminances

B) Establish the camera imaging distance optimization model

In the imaging process of TFW-TDB, the imaging method of vertical transmission of lens with surface is used, and the imaging distance L directly affects the depth of field ΔL of imaging, that is, the overlap thickness of TFW-TDB. We suppose that the maximum thickness of a single TFW-TDB is H, and the overlapping thickness of TFW-TDB in the sorting process does not exceed m layers, the following equation needs to be satisfied:

$$\Delta L \geq （m + \lambda） H \tag{3}$$

where, λ is the compensation factor for camera installation error and other effects, through the experiment to take λ = 0.5. TFW-TDB will be placed on the conveyor belt for several experiments can be known m = 3. Assume that the camera shooting aperture value is F, the lens focal length is f. From the imaging principle of camera, it is known that the camera depth of field ΔL, focal length f, aperture value F satisfy the following formula:

$$\begin{cases} \Delta L_1 = \dfrac{FdL^2}{f^2 + FdL} \\ \Delta L_2 = \dfrac{FdL^2}{f^2 - FdL} \end{cases} \tag{4}$$

Simplify above:

$$\Delta L = \Delta L_1 + \Delta L_2 = \frac{\alpha L^2}{\beta + \alpha L} + \frac{\alpha L^2}{\beta - \alpha L} \tag{5}$$

where, ΔL_2 is the depth of field, $\alpha = F \cdot d$, $\beta = f^2$, d is the allowable dispersion circle diameter and the camera frame, based on the size of the camera imaging frame in the experiment (480×360 mm) and the literature [40] can be known, we take d = 0.146.

From Eq. 3 and Eq. 4 can be established Eq. 5 to find the camera imaging distance L need to meet the Eq. 6:

$$L \geq \left(\frac{(m+\lambda) H\beta^2}{2\alpha\beta + (m+\lambda) H\alpha^2}\right)^{\frac{1}{2}} \tag{6}$$

It is known from the imaging theory that when the imaging distance is reduced, the pixel density occupied by the TFW-TDB imaging target features is higher and the recognition accuracy is higher, so the minimum value of Eq. 6 can be taken as the optimal imaging distance.

2.3 TFW-TDB visual recognition

Construction of a flexible target matching template

Template matching algorithm is an effective method to achieve target feature localization. Due to the existence of flexible deformation and other characteristics of the infusion tube drip bucket, it causes the traditional rigid workpiece matching template construction algorithm to be difficult to apply. This study adopts a global-local contour line fusion matching template construction method, and the related theory and algorithm are as follows.

A) Image pre-processing

Due to the factors such as the imaging environment lighting, TFW-TDB itself material inhomogeneity, there is noise in the imaging process of TFW-TDB, it is necessary to perform certain preprocessing operations on TFW-TDB image to eliminate the noise and initially filter the infusion tube drip bucket which is not qualified in shape and color or has serious deformation, the related algorithm is as follows:

(1) If the pixel values of any pixel point $P(i,j)$ in Image_1 in R,G,B channels before preprocessing are $P_R(i,j)$, $P_R(i,j)$, $P_B(i,j)$, respectively, and the value after binarization is $P_{Gray}(i,j)$, the calculation formula for binarization of Image_1 is as follows:

$$P_{Gray}(i,j) = a_1 \cdot P_R(i,j) + b_1 \cdot P_G(i,j) + c_1 \cdot P_B(i,j) \tag{7}$$

where, a_1, b_1, c_1 are the weight coefficients of R, G, B triple pass at the time of binarization. The information entropy is used as the evaluation index of imaging quality after binarization, and the a_1,b_1,c_1 weights are obtained when the information entropy of TFW-TDB Image_1 is maximized after binarization, and then a_1 = 0.299, b_1 = 0.587, c_1 = 0.114 are determined by fitting with the least squares method. The TFW-TDB region after binarization is shown in Fig. 3(a). The TFW-TDB region is shown in Fig. 3(b) after binarization of Image2 with grayscale inversion.

(2) The two ends of TFW-TDB show irregular deformation. When the TFW-TDB image matching template is established, under the condition that the rectangular region of interest (ROI) completely contains the bubble chambers to the left and right of TFW-TDB, considering that the bubble chambers to the left and right of TFW-TDB have small deformation relative to the spatial position in the actual process, the rectangular region of interest (ROI) shown in Fig. 3(c) is set as the boundary line by deviating 10 pixel points from the bubble chambers to the left and right of TFW-TDB, and the irregular ends of the standard sample are removed to segment the feature region as shown in Fig. 3(d).

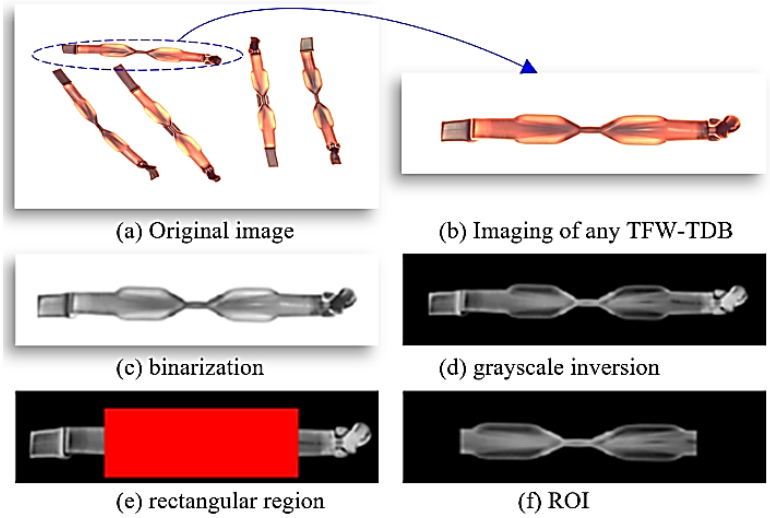

Fig. 3 Preprocessing images

B) Creating templates

TFW-TDB will cause small deformation easily between the left and right bubble chambers in the overlapping state, but the left and right bubble chambers themselves do not change shape easily, the method of global-local contour line feature fusion is used to create the TFW-TDB matching template (shown in Fig. 4). The matching template contains two parts of features, the global features are two global contour lines in red and purple, and the local features are four local contour lines in green, blue, light blue and yellow. The global contour lines are clear and complete, reflecting the main features of the infusion tube valve bubble. The local contour lines reflect the structure of the two bubbling chambers and present an asymmetric structure, which can prevent a template from repeatedly matching the same workpiece.

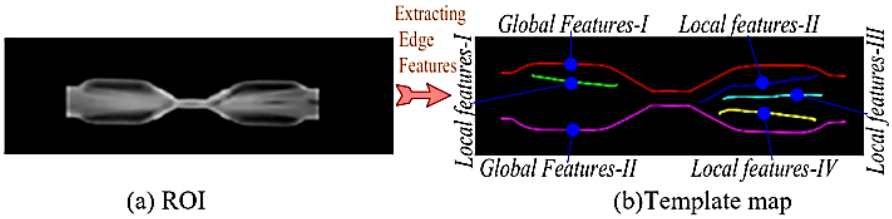

Fig. 4 Template map

TFW-TDB matching algorithm and implementation

Achieving the matching of TFW-TDB features with the created template is one of the key steps to realize the irregular TFW-TDB image localization, and the recognition algorithm based on template matching is developed for the features of TFW-TDB and the above created template as follows:

Step1: Using the above image pre-processing algorithm, the $Image_1$ is binarized and grayscale inversion operation is performed to obtain image $Image_2$.

Step2: Using morphological algorithm to denoise $Image_2$ is to obtain $Image_3$, based on which the number t of corresponding single or overlapping TFW-TDB is identified in conjunction with the connected domain algorithm, and the identified TFW-TDB are segmented and encoded, where any one segmentation region is noted as $Image_{3\text{-}j}$ $(j = 1, 2, \ldots, t)$.

Step3: The matching template operator in the literature [29] is used, and the search greediness parameter is set to 0.9, the minimum threshold score parameter is between 0.5 and 0.55, the overlap coefficient is 0.3, and the maximum number of matches parameter is calculated as follows:

$$N = \frac{S_{roi}}{S_{unit}} + 1 \tag{8}$$

where, S_{roi} is the area of the region, S_{unit} is the area reference value of a single workpiece, the output result of the matching template operator is the row coordinate Row_j, column coordinate $Column_j$, rotation angle $Angle_j$, scaling $Scale_j$, matching $score_j$ of the upper left vertex of any TFW-TDB$_j$ of the rectangular image Image$_{4\text{-}j}$ matched in Image$_1$. This matrix carrying the template matching pose information is then applied to the template contour image to form the matching contour image, and the matching effect is shown in Fig. 5.

Step4: Since the result of TFW-TDB matching may have deviation, it needs to be corrected. First, take the minimum outer rectangle of any TFW-TDB$_j$ matching contour line as in Fig. 6(a); then merge the rectangle shapes, and then take the minimum outer rectangle on the basis of the merged shapes as in Fig. 6(b), and output the minimum outer rectangle row coordinates of the upper left vertex of TFW-TDB$_j$ Image$_{4\text{-}j}$ matching after correction Row_j', column coordinates $Column_j'$, rotation angle $Angle_j'$, outer rectangle length and width respectively are $Lenght_0'$, $Width_0'$.

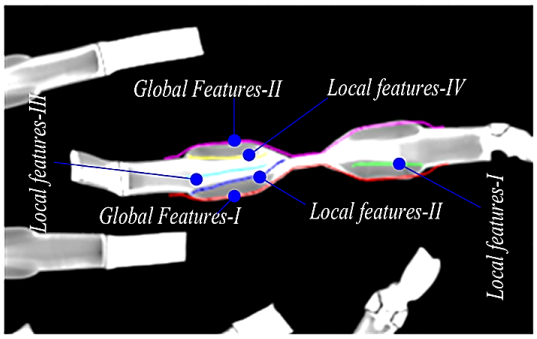

Fig. 5 Matching effect display

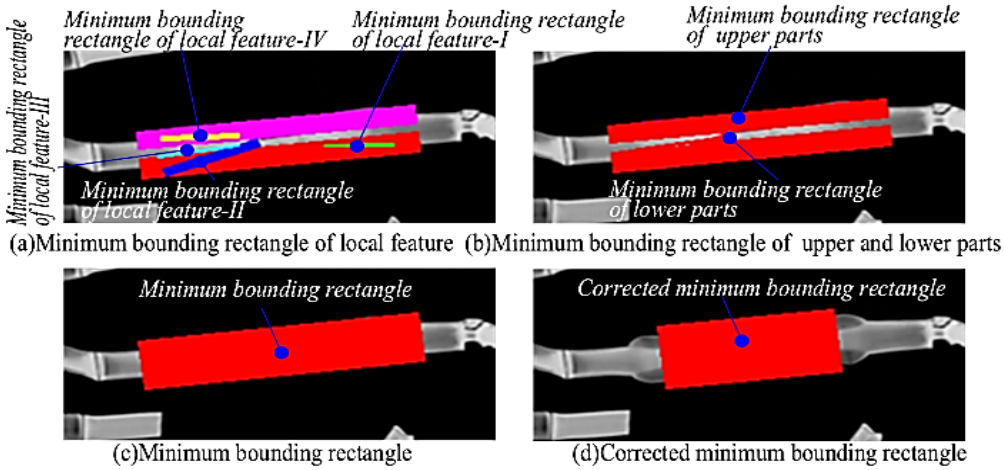

Fig. 6 Matching result correction

Establishing TFW-TDB spatial overlap state discriminant model

After image processed, the planar coordinates and rotation angle of the TFW-TDB on the conveyor belt can be accurately obtained, but the characteristics of the TFW-TDB such as translucency and overlap make it difficult to obtain the height information on the conveyor belt, which restricts the realization of automated sorting and assembly of the TFW-TDB. Therefore, spatial determination of the overlap where the TFW-TDB is located is needed. This study establishes a coupling model between the overlapping layer and the imaging quality of TFW-TDB, and identifies the overlapping layer of TFW-TDB by its imaging quality.

A) Constructing the overlap region of interest model

The positioning of feature points in the left and right bubble chambers of TFW-TDB is the key factor to realize its sorting and assembly, however, the complete imaging and segmentation accuracy of the left and right bubble chambers of TFW-TDB determine the accuracy and reliability of TFW-TDB positioning. The corrected matching area can accurately locate the area where TFW-TDB is located, but the complete imaging of TFW-TDB left and right bubble chambers is incomplete. Therefore, the corrected matching area is used as the basis to construct the overlap area of interest, which provides the image basis for the analysis of the overlap layer where TFW-TDB is located. If the percentage of the aligned contour lines in the TFW-TDB image along the length and width directions is $H_1\%$, $W_1\%$, respectively, and the extension rate of TFW-TDB in the length and width directions is $H_2\%$, $W_2\%$, respectively, and the length and width of the outer truncated rectangle of the matching template are $Length_0$, $Width_0$, respectively, the row coordinates Row_j', column coordinates $Column_j'$, rotation angle $Angle_j'$ of the upper left vertex of the TFW-TDB overlapping rectangle region of interest, the outer truncated rectangle .

The length and width are $Lenght_0'$, $Width_0'$ respectively, then the parameters of TFW-TDB$_j$ overlapping region of interest (ROI_j) are calculated as shown in Eq. 9.

$$\begin{cases} \dfrac{Row_j^{ROI} - Row_j'}{0.5 \cdot (Length_j^{ROI} - Length_j')} = \cos\left(Angle_j^{ROI}\right) \\ \dfrac{Column_j^{ROI} - Column_j'}{0.5 \cdot (Width_j^{ROI} - Width_j')} = \sin\left(Angle_j^{ROI}\right) \\ Length_j^{ROI} = \dfrac{Length_0 \cdot Scale_j \cdot (1 + H_2\%)}{H_1\%} \\ Width_j^{ROI} = \dfrac{Width_0 \cdot Scale_j \cdot (1 + W_2\%)}{W_1\%} \\ Angle_j^{ROI} = Angle_j' \end{cases} \tag{9}$$

In the experiment, the percentage of TFW-TDB images along the length and width directions $H_1\%$, $W_1\%$ are 80 % and 95 %, respectively. The extension rate of TFW-TDB in the length and width directions $H_2\%$, $W_2\%$ are 20 % and 5 %, respectively. The overlap region of interest of TFW-TDB$_j$ is shown in Figs. 7 and 8 when the value is taken into Eq. 9.

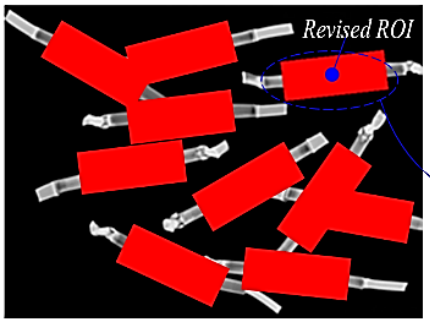

Fig. 7 Region of interest

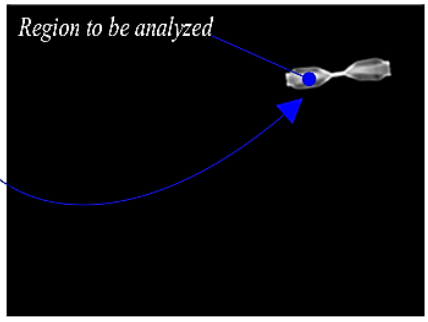

Fig. 8 Overlapping analysis area

B) Establishing an overlap layer discrimination model based on imaging quality

In the TFW-TDB overlap region of interest, the Sobel operator is applied to extract the edge features in the left and right bubble chambers of the TFW-TDB, shown in Fig. 9.

(a) Edge extraction of unoverlapped regions (b) Edge extraction of overlapping regions

Fig. 9 Edge extraction

As can be seen from the figure, the TFW-TDB is imaged after overlapping, the upper layer features are clear and the lower layer features are blurred, so the feature imaging quality evaluation function of the TFW-TDB can be constructed, and then the spatial layer in which the TFW-TDB is located is coupled with the feature imaging quality model, which works as follows.

(1) The feature imaging quality evaluation function of TFW-TDB was constructed. When TFW-TDB is overlapped, there are certain differences in the imaging clarity of upper and lower TFW-TDB and the contrast of TFW-TDB features in the image. Therefore, the sharpness coefficient *Sharpness* and information *Entropy* are used as the feature imaging quality evaluation index of TFW-TDB in ROI_j.

First, the image variance is calculated in ROI_j of TFW-TDB$_j$ and flipped in the interval [0, 100] to obtain the sharpness coefficient $Sharpness_j$ of TFW-TDB$_j$, which is calculated by the equation:

$$Sharpness_j = 100 - \sqrt{\frac{\sum_{p=1}^{n}\left(g(p) - \sum_{p=1}^{n} g(p)/n\right)^2}{n}} \tag{10}$$

where, p is any pixel point within ROI_j, $g(p)$ is the gray value of p, and n is the total number of ROI_j pixel points. Secondly, the information entropy is calculated at ROI_j of TFW-TDB$_j$, which is given by:

$$Entropy_j = \sum_{p=1}^{n}\left(g(p_k) \cdot \log_2 g(p_k)\right) \tag{11}$$

where, p_k denotes the probability that the grayscale value is k. The calculated sharpness coefficients are normalized and multiplied by the weighting factor α. The information entropy is also multiplied by the weighting factor β, and then summed up to obtain the imaging quality assessment coefficient $OverlapScore_j$ of TFW-TDB$_j$ as follows.

$$OverlapScore_j = \alpha \cdot \frac{Sharpness_j}{100} + \beta \cdot Entropy_j \tag{12}$$

(2) Establishing the spatial layer discriminant rule for TFW-TDB. When TFW-TDB$_i$, TFW-TDB$_j$ is identified in the image and judged to be overlapping, the discriminative rules for the spatial location of the upper and lower layers of TFW-TDB$_i$, TFW-TDB$_j$ are shown in the following terms.

$$\begin{aligned} &OverlapScore_i > OverlapScore_j, \textit{ TFW-TDB}_i \textit{ is} \text{ located on the upper layer} \\ &\text{else, } \textit{TFW-TDB}_j \text{ is located on the lower layer} \end{aligned} \tag{13}$$

3. Experimental results and analysis

3.1 Experimental method

To verify the above theory and model, an experimental platform was built as shown in Fig. 10, in which a Daheng 5-megapixel USB3.0 interface CCD (MER-500-7UC) was used, and the auxiliary light source was illumination system using a red surface array light source (TSD-FL300200FRLED) and a digital light source controller (TSD-DPA6024V-2S). The experimental process is as follows:

- To place a transparent glass plate above the surface array light source for simulating a transparent conveyor belt.
- Selecting a batch of TFW-TDB to be identified at any time and putting them onto the upper surface of the transparent glass plate, so that there is no overlap, overlap and other phenomena.
- Simulate the change of TFW-TDB density on the conveyor belt during the recognition process by increasing and decreasing TFW-TDB and simulate the random overlapping state by changing the overlapping posture of TFW-TDB.
- The camera acquires images of TF0W-TDB workpieces containing no overlap and with overlap in the random state.
- The images are processed by the algorithm in this study to identify the image positioning coordinates of TFW-TDB and the overlapping layer they are in.

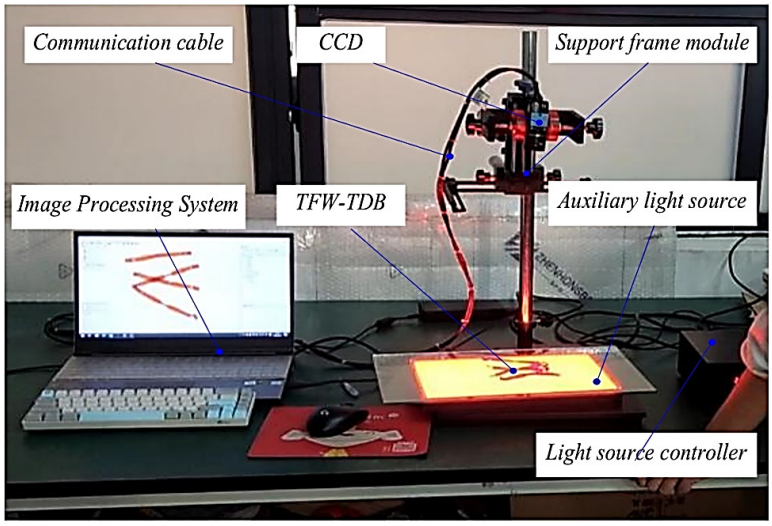

Fig. 10 Experimental setup diagram

3.2 Data sets

In the actual working condition, the variation of the surrounding light intensity is strong, in order to overcome the environmental defects and improve the robustness, accuracy and efficiency of the reliability of the algorithm, 300 samples of TFW-TDB images under different lighting environments are collected in this paper, which contain different ambient lighting, no overlap and with overlap. The relevant sample data are shown in Table 1.

Table 1 Composition of training set and test set

	Low light environment	Medium light environment	Intense light environment
No overlap	1494	1240	1125
Overlap	1494	1240	1125

3.3 Evaluation indicators

In order to objectively evaluate the recognition results of different methods in the overlapping layer where TFW-TDB is located, four evaluation indexes are used: Recall value, Precision value, F-measure value, and FPS value, which are calculated as follows: manually mark the actual overlapping layer where TFW-TDB is located, the total number of which is defined as NP, mark the predicted as upper layer, the actual also in the upper layer is marked as TP, predicted as the lower layer, actually the upper layer is marked as FP, predicted as the lower layer, actually also the lower layer is marked as TN, predicted as the lower layer, actually the upper layer is marked as FN. in addition, when there is no overlap in TFW-TDB, it is recorded as the upper layer.

- Recall and Precision: Given an IoU threshold, two parameters, Recall and Precision can be determined. If the true value of IoU and ground overlap of the bounding box exceeds 0.5, Recall R and Precision P are expressed as follows:

$$\begin{cases} R = \dfrac{TP}{NP} = \dfrac{TP}{TP + FN} \\ P = \dfrac{TP}{TP + FP} \end{cases} \tag{14}$$

- $F_{measure}$ value: $F_{measure}$ value is the weighted value of precision and recall, and its equation is as follows:

$$F_{measure} = \frac{(1 + \alpha) \cdot P \cdot R}{\alpha \cdot P + R} \tag{15}$$

where, α is a non-negative real number that represents the weighting factor between precision and recall, which in our work is empirically set to 0.8 [22]. It is important to note that the higher the value of $F_{measure}$, the better the performance of our method.

- FPS value (Frame Per Second): In addition to the accuracy of TFW-TDB upper and lower recognition, another important performance index of TFW-TDB recognition algorithm is speed, only fast can achieve real-time detection, which is extremely important for some application scenarios. A common metric to evaluate the speed is Frame Per Second (FPS), which is the number of TFW-TDB that can be processed in each second.

3.4 Experimental data and analysis

Develop TFW-TDB visual recognition algorithm and localization system with the help of OpenCV, C# and other software platforms. In this system, the calibration method in the literature [43] is used to calibrate the internal and external parameters of the camera, and the optimal imaging distance $L = 100$ of the camera is solved based on the obtained information of the internal and external parameters of the camera by Eq. 3. Then, the proposed algorithm is used to realize the binarization of the image and ROI region acquisition and create the matching template. Secondly, the proposed matching algorithm is used to realize the TFW-TDB. Finally, the image coordinate system OUVW is established with the top left of the image as the origin, the horizontal direction as the V-axis and the vertical direction as the U-axis, and the coordinates of the center point of the right bubble chamber of TFW-TDB and the angle with the V-axis are identified and output, the imaging quality evaluation coefficient, and part of the identification results are shown in Fig. 11.

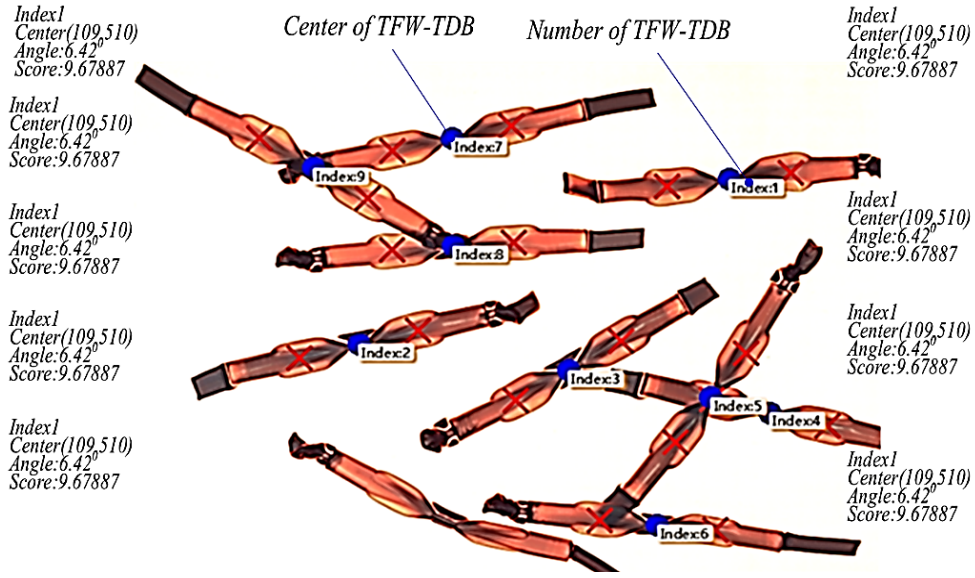

Fig 11 Experimental setup diagram

Initially, the coordinate center information of the TFW-TDB left and right bubble center images are located in the sample image. Then, the image positioning coordinate center information of the left and right bubble centers of TFW-TDB in the sample image is extracted by our method. Finally, the errors of the two recognition results are calculated as shown in Fig. 12. The recognition result of the algorithm in this paper has been basically with the manually one. For some of the waste material in the workpiece, the results have large differences in the deformation between the left and right bubble chamber, resulting the calculation results by our method are zero. Similar identification results can be used as a basis for rejecting scrap.

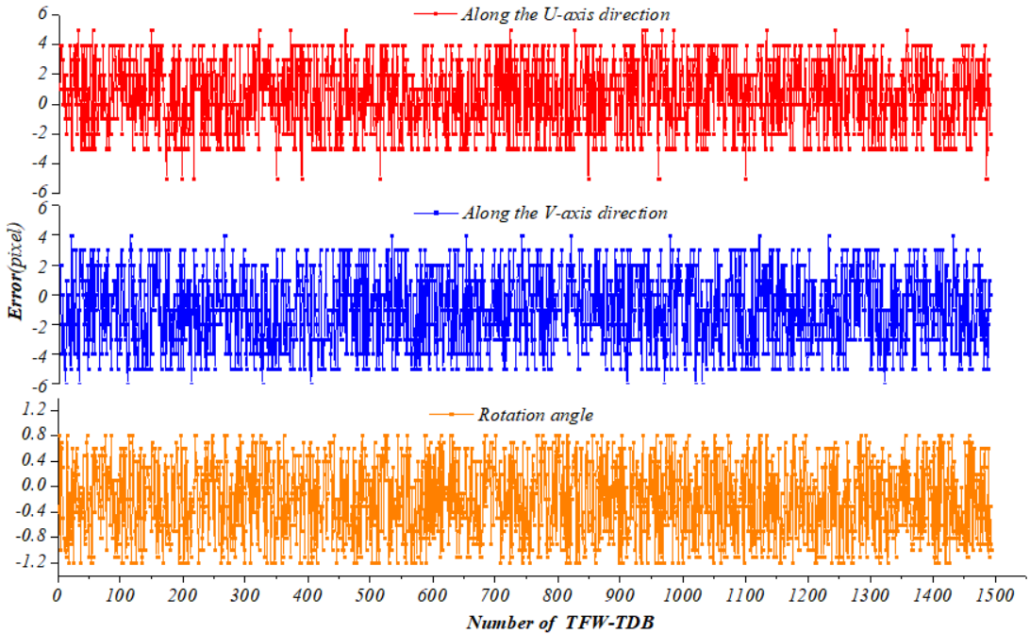

Fig 12 Error of recognition results

Table 2 Results of different algorithms for identifying the layer of TFW-TDB

		Our Method			the literature 35 algorithm			the literature 36 algorithm		
	Actual layer	Prediction layer Upper layer	Prediction layer Lower layer	Sample number	Prediction layer Upper layer	Prediction layer Lower layer	Prediction layer	Prediction layer Upper layer	Prediction layer Lower layer	Prediction layer
Low illumination	Upper layer	1238	3	1241	1237	4	1241	1235	6	1241
	Lower layer	4	249	253	3	250	253	5	248	253
	recall		82.86 %			82.80 %			82.66 %	
	precision		99.76 %			99.68 %			99.52 %	
	F-measure		91.47 %			91.40 %			91.25 %	
	FPS		10			8			9	
Medium illumination	Upper layer	1016	1	1017	1015	2	1017	1012	5	1017
	Lower layer	2	221	223	1	222	223	3	220	223
	recall		81.94 %			81.85 %			81.61 %	
	precision		99.90 %			99.80 %			99.51 %	
	F-measure		91.03 %			90.94 %			90.67 %	
	FPS		12			9			10	
High illumination	Upper layer	956	5	961	954	7	961	957	4	961
	Lower layer	5	186	191	4	187	191	8	183	191
	recall		82.99 %			82.81 %			83.07 %	
	precision		99.48 %			99.27 %			99.58 %	
	F-measure		91.41 %			91.21 %			91.50 %	
	FPS		9			7			7	

In this experiment, the upper and lower layers information in which the TFW-TDB annotations are located in the sample images is obtained manually. Then, the information such as the overlapping layers in which the TFW-TDB left and right bubbles are located in the sample images is extracted by using the literature [41] algorithm, the literature [42] algorithm, and the algorithm in

this paper, respectively, and the recognition results are shown in Table 2, which lists the recognition results under different lighting environments. For the properly illuminated environment, we identified a total of 1240 TFW-TDB from the 300 image samples obtained, among which two lower TFW-TDB were incorrectly identified as upper TFW-TDB. One upper TFW-TDB was incorrectly identified as lower TFW-TDB in 222 cases where lower TFW-TDB were identified. The F-measure of the sample was 91.03 %, which verified the validity of the method. We also compared our method with two state-of-the-art algorithms, the literature 35 algorithm and the literature [36] algorithm. Compared with our method, the literature 35 algorithm consumes 33 % more time and reduces the recall, accuracy and F-measure values by 0.11 %, 0.10 % and 0.09 %, respectively. Meanwhile, the literature 36 algorithm consumes 20 % more time and reduces the recall and accuracy by 0.40 %, 0.39 % and 0.40 %, respectively. The algorithm proposed in this paper achieves the computation of ground complexity based on guaranteed computational accuracy and reliability. Similar results are shown in dark and bright lighting environments, and it can be observed that our method still has stable performance in terms of recall, accuracy, and F-measure values as the ambient lighting changes.

4. Conclusion

Our paper presents an automatic spatial position recognition system for picking and assembly of translucent and flexible workpieces. For the spatial position recognition of TFW-TDB in the automatic sorting process, the imaging parameters are optimized by jointly using imaging modelling and translucent and flexible workpiece features, the ROI method and target matching algorithm are used to quickly acquire TFW-TDB in images and then complete image localization. However, the recognition algorithm based on machine vision has certain limitations. When the type of translucent and flexible workpiece changes, it is necessary to reset the edge matching features based on the specific characteristics of translucent and flexible workpieces, and the ROI region. In the future research, we will further explore the adaptive matching algorithm and adaptive ROI region algorithm to realize the intelligent extraction of spatial position of any type of translucent and flexible workpieces without human-machine interaction.

Acknowledgement

This paper was funded by Natural Science Foundation of Guangdong Province (2016A030310309); (2019A1515010961); Guangdong Science and Technology Department (2017A010102009); (2017B010118004); Science and Technology Project of Guangzhou Maritime University (G410203); Science and Technology Project of Guangzhou (201707010187); (201804010354); (PDJH2019a0367); (PDJH2019b0371).

References

[1] Tripathi, S., Shukla, S., Attrey, S., Agrawal, A., Bhadoria, V.S. (2020). Smart industrial packaging and sorting system, In: Kapur, P.K., Singh, O., Khatri, S.K., Verma, A.K. (eds.), *Strategic system assurance and business analytics,* Springer, Singapore, 245-254, doi: 10.1007/978-981-15-3647-2_18.

[2] Zhao, Z., Yuan, Q. (2022). Integrated multi-objective optimization of predictive maintenance and production scheduling: Perspective from lead time constraints, *Journal of Intelligent Management Decision*, Vol. 1, No. 1, 67-77, doi: 10.56578/jimd010108.

[3] Olscher, C., Jandric, A., Zafiu, C., Part, F. (2022). Evaluation of marker materials and spectroscopic methods for tracer-based sorting of plastic wastes, *Polymers*, Vol. 14, No. 15, Article No. 3074, doi: 10.3390/polym14153074.

[4] Lovich, M.A., Doles, J., Peterfreund, R.A. (2005). The impact of carrier flow rate and infusion set dead-volume on the dynamics of intravenous drug delivery, *Anesthesia & Analgesia*, Vol. 100, No. 4, 1048-1055, doi: 10.1213/01.ANE.0000146942.51020.88.

[5] Society, I.N. (2006). Infusion nursing standards of practice, *Journal of Infusion Nursing: The Official Publication of the Infusion Nurses Society*, Vol. 29, No. 1, doi: 10.1097/00129804-200601001-00001.

[6] Patel, P.J., Benasi, K., Ferrari, G., Evans, M.G., Shanmugham, S., Wilson, D.M., Buckingham, B.A. (2014). Randomized trial of infusion set function: Steel versus teflon, *Diabetes Technology & Therapeutics*, Vol. 16, No. 1, 15-19, doi: 10.1089/dia.2013.0119.

[7] Yu, J.H., Miao, W.J., Zhang, G.B., Li, K., Shi, Y.G., Liu, L. (2021). Target positioning and sorting strategy of fruit sorting robot based on image processing, *Traitement du Signal,* Vol. 38, No. 3, 797-805, doi: 10.18280/ts.380326.

[8] Adediran, E.M., Fadare, D.A., Falana, A., Kazeem, R.A., Ikumapayi, O.M., Adedayo, A.S., Adetunla, A.O., Ifebunandu, U.J., Fadare, D.A., Olarinde, E.S. (2023). UIArm I: Development of a low-cost and modular 4-DOF robotic arm for sorting plastic bottles from waste stream, *Journal Européen des Systèmes Automatisés*, Vol. 56, No. 1, 97-103, doi: 10.18280/jesa.560113.
[9] Kao, Y.-H., Chen, C.-K., Chen, C.-C., Lan, C.-Y. (2022). Object pose estimation and feature extraction based on PVNet, *IEEE Access*, Vol. 10, 122387-122398, doi: 10.1109/ACCESS.2022.3223695.
[10] Tang, Y., Chen, M., Wang, C., Luo, L., Li, J., Lian, G., Zou, X. (2020). Recognition and localization methods for vision-based fruit picking robots: A review, *Frontiers in Plant Science*, Vol. 11, Article No. 510, doi: 10.3389/fpls.2020.00510.
[11] Yang, J., Wang, C., Jiang, B., Song, H., Meng, Q. (2020). Visual perception enabled industry intelligence: State of the art, challenges and prospects, *IEEE Transactions on Industrial Informatics*, Vol. 17, No. 3, 2204-2219, doi: 10.1109/TII.2020.2998818.
[12] Minu, M.S., Aroul Canessane, R., Subashka Ramesh, S.S. (2022). Optimal squeeze net with deep neural network-based arial image classification model in unmanned aerial vehicles, *Traitement du Signal*, Vol. 39, No. 1, 275-281, doi: 10.18280/ts.390128.
[13] Xing, J., Jia, M. (2021). A convolutional neural network-based method for workpiece surface defect detection, *Measurement*, Vol. 176, Article No. 109185, doi: 10.1016/j.measurement.2021.109185.
[14] Mandracchia, B., Hua, X., Guo, C., Son, J., Urner, T., Jia, S. (2020). Fast and accurate sCMOS noise correction for fluorescence microscopy, *Nature Communications*, Vol. 11, Article No. 94, doi: 10.1038/s41467-019-13841-8.
[15] Li, H., von Kleist-Retzow, F.T., Haenssler, O.C., Fatikow, S., Zhang, X. (2019). Multi-target tracking for automated RF on-wafer probing based on template matching, In: *Proceedings of 2019 International Conference on Manipulation, Automation and Robotics at Small Scales (MARSS),* Helsinki, Finland, 1-6, doi: 10.1109/MARSS.2019.8860983.
[16] Shahzad, A.R., Jalal, A. (2021). A smart surveillance system for pedestrian tracking and counting using template matching, In: *Proceedings of 2021 International Conference on Robotics and Automation in Industry (ICRAI),* Rawalpindi, Pakistan, 1-6, doi: 10.1109/ICRAI54018.2021.9651452.
[17] Varma, R.K.P., Ganta, S., Krishna, B.H., Svsrk, P. (2020). A novel method for Indian vehicle registration number plate detection and recognition using image processing techniques, *Procedia Computer Science*, Vol. 167, 2623-2633, doi: 10.1016/j.procs.2020.03.324.
[18] Sreeja, N.K. (2023). A hierarchical heterogeneous ant colony optimization based fingerprint recognition system, *Intelligent Systems with Applications*, Vol. 17, Article No. 200180, doi: 10.1016/j.iswa.2023.200180.
[19] Li, Z., Xiao, Y., Wu, Q., Jin, M., Lu, H. (2020). Deep template matching for offline handwritten Chinese character recognition, *The Journal of Engineering*, Vol. 2020, No. 4, 120-124, doi: 10.1049/joe.2019.0895.
[20] Vukicevic, A., Mladineo, M., Banduka, N., Macuzic, I. (2021). A smart Warehouse 4.0 approach for the pallet management using machine vision and Internet of Things (IoT): A real industrial case study, *Advances in Production Engineering & Management*, Vol. 16, No. 3, 297-306, doi: 10.14743/apem2021.3.401.
[21] Ćirić, I., Pavlović, M., Banić, M., Simonović, M., Nikolić, V. (2022). AI powered obstacle distance estimation for onboard autonomous train operation, *Tehnički Vjesnik – Technical Gazette,* Vol. 29, No. 2, 611-619, doi: 10.17559/TV-20210223081612.
[22] Kapetanidis, V., Michas, G., Spingos, I., Kaviris, G., Vallianatos, F. (2023). Cluster analysis of seismicity in the eastern gulf of corinth based on a waveform template matching catalog, *Sensors*, Vol. 23, No. 6, Article No. 2923, doi: 10.3390/s23062923.
[23] Korman, S., Reichman, D., Tsur, G., Avidan, S. (2013). FasT-match: Fast affine template matching, In: *Proceedings of 2013 IEEE Conference on Computer Vision and Pattern Recognition,* Portland, USA, 2331-2338, doi: 10.1109/CVPR.2013.302.
[24] Zhang, Y., Zhang, Z., Peng, S., Li, D., Xiao, H., Tang, C., Miao, R., Peng, L. (2022). A rotation invariant template matching algorithm based on Sub-NCC, *Mathematical Biosciences and Engineering*, Vol. 19, No. 9, 9505-9519, doi: 10.3934/mbe.2022442.
[25] Zhang, Z., Yang, X., Jia, X. (2021). Scale-adaptive NN-based similarity for robust template matching, *IEEE Transactions on Instrumentation and Measurement*, Vol. 70, Article No. 5002809, doi: 10.1109/TIM.2020.3028401.
[26] Ye, Y., Bruzzone, L., Shan, J., Bovolo, F., Zhu, Q. (2019). Fast and robust matching for multimodal remote sensing image registration, *IEEE Transactions on Geoscience and Remote Sensing*, Vol. 57, No. 11, 9059-9070, doi: 10.1109/TGRS.2019.2924684.
[27] Wu, Y., Li, Q. (2022). The algorithm of watershed color image segmentation based on morphological gradient, *Sensors*, Vol. 22, No. 21, Article No. 8202, doi: 10.3390/s22218202.
[28] Wang, S., Wang, H., Zhou, Y., Liu, J., Dai, P., Du, X., Wahab, M.A. (2021). Automatic laser profile recognition and fast tracking for structured light measurement using deep learning and template matching, *Measurement*, Vol. 169, Article No. 108362, doi: 10.1016/j.measurement.2020.108362.
[29] Hikosaka, S., Tonooka, H. (2022). Image-to-image subpixel registration based on template matching of road network extracted by deep learning, *Remote Sensing*, Vol. 14, No. 21, Article No. 5360, doi: 10.3390/rs14215360.
[30] Chen, D., Hu, F., Mathiopoulos, P.T., Zhang, Z., Peethambaran, J. (2023). MC-UNet: Martian crater segmentation at semantic and instance levels using u-net-based convolutional neural network, *Remote Sensing*, Vol. 15, No. 1, Article No. 266, doi: 10.3390/rs15010266.
[31] Sangeetha, D., Deepa, P. (2019). FPGA implementation of cost-effective robust Canny edge detection algorithm, *Journal of Real-Time Image Processing*, Vol. 16, 957-970, doi: 10.1007/s11554-016-0582-2.

[32] Navdeep, K., Goyal, S., Rani, A., Singh, V. (2019). An improved local binary pattern based edge detection algorithm for noisy images, *Journal of Intelligent & Fuzzy Systems*, Vol. 36, No. 3, 2043-2054, doi: 10.3233/JIFS-169916.
[33] Mittal, M., Verma, A., Kaur, I., Kaur, B., Sharma, M., Goyal, L.M., Roy, S., Kim, T.H. (2019). An efficient edge detection approach to provide better edge connectivity for image analysis, *IEEE Access*, Vol. 7, 33240-33255, doi: 10.1109/ACCESS.2019.2902579.
[34] He, S., Ye, B., Li, H., Gao, Y. (2022). Recognition of disordered workpieces based on 3D Laser scanner and RS-CNN, In: *Proceedings of 2022 21st International Symposium on Distributed Computing and Applications for Business Engineering and Science (DCABES)*, Chizhou, China, 62-65, doi: 10.1109/DCABES57229.2022.00052.
[35] Chen, L., Zhong, G., Han, Z., Li, Q., Wang, Y., Pan, H. (2022). Binocular visual dimension measurement method for rectangular workpiece with a precise stereoscopic matching algorithm, *Measurement Science and Technology*, Vol. 34, No. 3, Article No. 035010, doi: 10.1088/1361-6501/aca707.
[36] Wang, W. (2019). A novel rapid point-cloud surface reconstruction algorithm for laser imaging radar, *Multimedia Tools and Applications*, Vol. 78, 8737-8749, doi: 10.1007/s11042-018-6244-6.
[37] Han, W., Han, X. (2022). Stack workpieces recognition model based on deep learning, In: *Proceedings of 2022 11th International Conference of Information and Communication Technology (ICTech),* Wuhan, China, 209-213, doi: 10.1109/ICTech55460.2022.00049.
[38] Li, S., Li, B., Wang, T., Dong, Z., Wang, Y., Huang, H. (2022). Research on cluttered object recognition algorithm based on improved YOLO V5, In: *Proceedings of 2022 5th World Conference on Mechanical Engineering and Intelligent Manufacturing (WCMEIM),* Ma'anshan, China, 1005-1009, doi: 10.1109/WCMEIM56910.2022. 10021373.
[39] Zhou, J., Wang, Y., Zhang, W. (2022). Underwater image restoration via information distribution and light scattering prior, *Computers and Electrical Engineering*, Vol. 100, Article No. 107908, doi: 10.1016/j.compeleceng.2022.107908.
[40] Li, M.Z., Wang, J.C., Jawarneh, M., Bhatt, M.W., Omarov, B., Raffik, R. (2023). Research on nonlinear tracking and evaluation of sports 3D vision action, *Nonlinear Engineering*, Vol. 12, No. 1, Article No. 20220243, doi: 10.1515/nleng-2022-0243.
[41] Xu, X., Wang, Y., Tang, J., Zhang, X., Liu, X. (2011). Robust automatic focus algorithm for low contrast images using a new contrast measure, *Sensors*, Vol. 11, No. 9, 8281-8294, doi: 10.3390/s110908281.
[42] Kobayashi, M., Ohmura, M., Takahashi, H., Shirai, T., Sakurai, K., Ichikawa, T., Yuzurihara, H., Inoue, S. (2018). High-definition and high-sensitivity CMOS image sensor with all-pixel image plane phase-difference detection autofocus, *Japanese Journal of Applied Physics*, Vol. 57, No. 10, Article No. 1002B5, doi: 10.7567/JJAP.57.1002B5.